Ultrafast Science
A SCIENCE PARTNER JOURNAL

RESEARCH ARTICLE

Gas and Droplet Dynamics for Filament-Assisted Free-Space Optical Communication through Clouds

Haiyi Liu[1], Jiawei Zheng[2], Huanyu Li[2], Jiayun Xue[1], Pengfei Qi[1*], Xianzhu Liu[2,3*], Lie Lin[1], Weiwei Liu[1], and Huilin Jiang[2,3]

[1]Tianjin Key Laboratory of Micro-scale Optical Information Science and Technology, Tianjin 300350, China. [2]College of Opto-Electronic Engineering, Changchun University of Science and Technology, Changchun 130022, China. [3]National and Local Joint Engineering Research Center of Space Optoelectronics Technology, Changchun University of Science and Technology, Changchun 130022, China.

*Address correspondence to: qipengfei@nankai.edu.cn (P.Q.); liuxianzhu@cust.edu.cn (X.L.)

Citation: Liu H, Zheng J, Li H, Xue J, Qi P, Liu X, Lin L, Liu W, Jiang H. Gas and Droplet Dynamics for Filament-Assisted Free-Space Optical Communication through Clouds. *Ultrafast Sci.* 2024;4:Article 0075. https://doi.org/10.34133/ultrafastscience.0075

Submitted 14 June 2024
Revised 8 August 2024
Accepted 2 September 2024
Published 2 October 2024

Femtosecond laser filamentation has recently emerged as a promising technique to actively create a channel through clouds and fog, thereby providing a revolutionary opportunity to overcome the obstacle of fog-induced attenuation for free-space optical communication (FSOC) in atmosphere. However, the underlying physics remains elusive, which is critical for optimizing time window and efficiency of guiding light in this channel. In this work, the time evolution of the filament-induced channel is investigated under various laser pulse energies and repetition rates. The combined diffusion model is built to reveal the contributions of gas molecules and aerosol droplets in competition of guiding and defocusing effect of the filament-induced channel. The related findings can deepen our understanding on the underlying physics of the air channel induced by the filament, provide insight into the optimizing time window and efficiency of guiding light, and potentially contribute to the improvement of filament-assisted FSOC.

Introduction

Free-space optical communication (FSOC) [1] utilizing infrared or visible light as carriers has recently been gaining substantial interest for real-world deployment [2,3] in both classical [4–6] and quantum [7–10] systems. Compared with conventional communication in radio frequencies, FSOC promises much higher single-channel bandwidth, as well as spatial confinement and interference immunity that improve security of information transmission [11,12]. FSOC has garnered substantial interest for communications between satellites and Earth ground stations [6,13], and between Earth and drones [6,10]. For example, China Aerospace Agency has successfully demonstrated long-distance quantum key distribution between the orbiting satellite and ground stations separated by distances of up to 1,200 km [9]. NASA has also utilized laser communications to transmit data over 30 million kilometers from the Psyche spacecraft to Earth, reaching data rates nearly 100 times faster than traditional radio frequency links, which will enable complex Mars missions [14,15]. However, FSOC's viability is critically restricted by signal attenuation in the presence of harsh environment such as fog, clouds, and haze. Mitigation tactics ranging from high-power CO_2 laser cleaning [16,17] to multiplication of networked ground stations have aimed to reduce opacity but carry disadvantages like high energy cost and system complexity, respectively.

Fortunately, the emergence of terawatt-class femtosecond lasers provides a revolutionary opportunity and scheme, filament-assisted FSOC, by actively creating an air channel through opacity by femtosecond laser filamentation for on-demand connection [18]. As the peak power of the ultrashort laser pulse surpasses a critical threshold, balance of focusing (Kerr effect) and defocusing (Kerr saturation, plasma generation) nonlinearities in propagation leads to the laser pulses maintaining a tightly confined beam width over a long propagation distance (ranging from centimeters to kilometers) far exceeding the diffraction length scale, that is, filamentation [19–27]. Notably, optical filaments exhibit minimal attenuation even in opaque conditions like fog or cloud cover [28–31], due to self-healing mechanism stemming from the intense background energy reservoir, which continually refuels the plasma core [30,32]. By drilling a nearly nondiffracting filament path through dense fog, the induced plasma and shockwave create a long, transparent "waveguide" by ejecting water droplets within the channel. A secondary communication beam centered in this channel can propagate with vastly reduced scattering and absorption compared to the background fog, dramatically extending the viable transmission distance of FSOC systems. Therefore, this unique atmospheric manipulation heightens prospects for real-world FSOC viability and attracts growing interest [18,33,34]. In past decade, a stationary high-speed communication channel with 30-fold increased optical transmission through fog

was established using femtosecond laser at kilohertz repetition rate [18], and 1.25 Gb/s video communication was obtained with the help of automatic gain control in a 6-dB-attenuated artificial cloud chamber [35].

Experimental validation has confirmed that high repetition rate laser filaments can effectively clear a quasi-steady and low loss channel through clouds, and the creation of a robust channel in fog for communication lasers via filamentation remains an active research area [18,34]. Addressing this challenge, the complexity of the underlying physics, specifically the diffusion dynamics of the multiscale and multiphase system activated by femtosecond laser filamentation, including gas molecules and droplets, remains to be fully elucidated. The physical scenario describing the femtosecond laser pulse propagation through water clouds consists of various processes in different spatial and temporal scales, such as light absorption, nonlinear ionization, molecule dissociation, plasma formation, and mechanical and thermal events including phase transition, shock-wave emission, thermal diffusion, and molecule and droplet diffusion. These processes determine the time window that the transparency is enhanced, which is very critical for the performance of filament-assisted FSOC.

In this work, we explore the time evolution of the filament-induced channel in fog under different laser energies and repetition rates, and develop a multiscale, multiphase diffusion model to elucidate the experimental observations. The guiding or defocusing of probe light is determined by the diffusion dynamics of gas molecules and droplets: For the atmosphere without aerosol, the induced channel via filamentation gives rise to light defocusing due to the thermal lensing effect arising from laser-induced air heating along the filament path; with the presence of aerosol, the induced channel can observably reduce the light attenuation from Mie scattering and guide the light. These findings could deepen our understanding on the underlying physics of the air channel induced by the filament, provide insights for optimizing time window and efficiency of guiding light, and potentially contribute to the improvement of filament-assisted FSOC.

Materials and Methods

Figure 1 illustrates the schematic diagram of experimental setup for investigating the formation and relaxation dynamics of channels induced by femtosecond laser filamentation. A commercial femtosecond laser system (Legend Elite, Coherent Inc.) delivers laser pulses with pulse duration of 60 fs, central wavelength of 800 nm, and maximum pulse energy of 3.5 mJ. The laser energy can be controlled with a half-wave plate (HWP) and polarizing beam splitter (PBS). Then, the femtosecond laser beam is incident on the telescope system composed of concave and convex lenses through a dielectric mirror and a dichroic mirror to precisely control femtosecond laser filamentation at desired target distances inside a cloud chamber. The diameter of cloud chamber is 4 cm, and aerosol, which is a suspension of water droplets in air, is introduced into the cloud chamber to simulate the effects of real-world cloud droplets on optical communication, providing an experimental emulation of atmospheric conditions that influence light transmission. The photograph of the filament is exhibited in the left inset of Fig. 1, the filament is formed at the distance of 2 m, and the filament length is about 15 cm. The electron density of the filament is estimated to be ~10^{16} cm^{-3} [21]; thus, the filament plasma frequency is calculated to be $\omega_p = \sqrt{4\pi n_e^2 / m_e \varepsilon_0} = 5.6$ GHz. The parameters within the formula are self-explanatory. Additionally, the 532-nm continuous-wave (CW) laser, designated as the probe beam, is utilized to simulate the communication beam in the filament-assisted

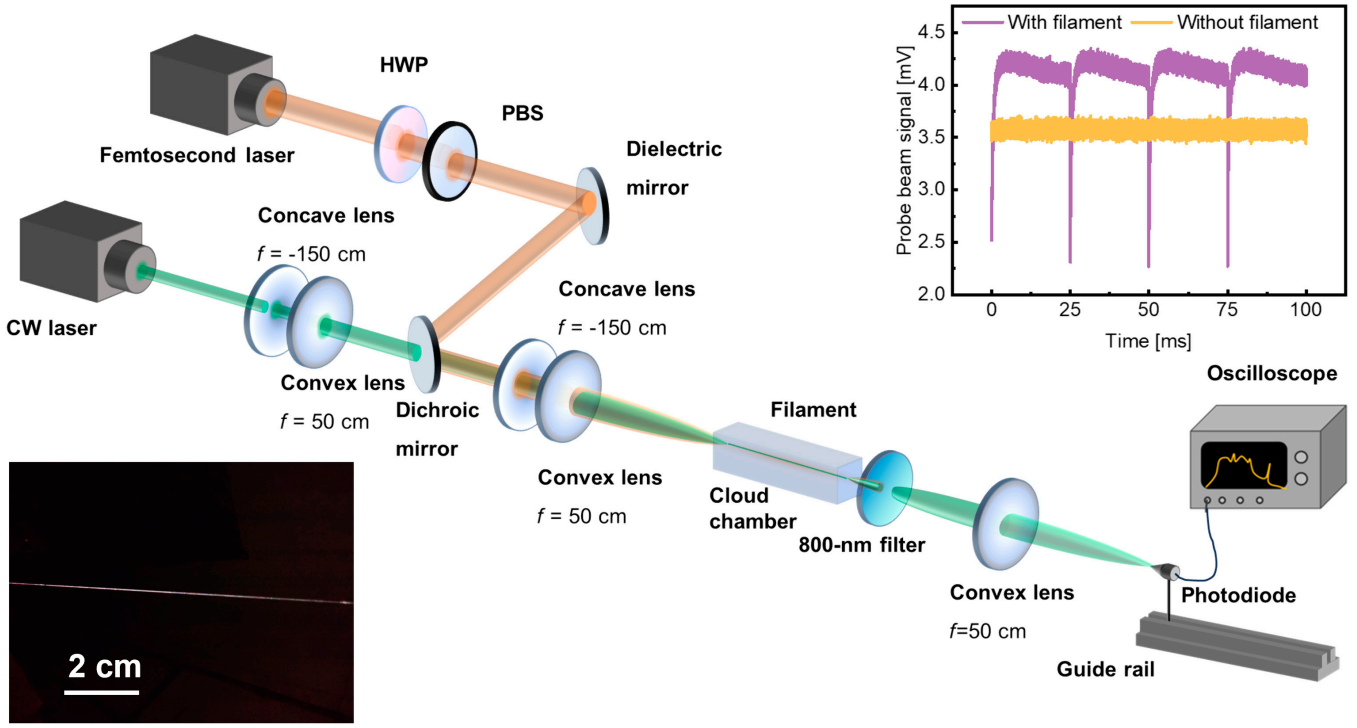

Fig. 1. Experimental setup for gas and droplet dynamics of channels induced by femtosecond laser filamentation. Insets: Photograph of filament (left) and evolution of probe beam (right).

FSOC scenario. The modulation of the probe beam's intensity enables directly assessing the transmission efficiency of the filament-induced channel. It is important to note that within the atmospheric channel, the thermal lensing effects as well as the defocusing effects are not sensitive to the wavelength variations. The laser with wavelength of 532 nm has been employed as the probe beam in previous literatures [18,33,34]. It indicates that using a 532-nm laser as a probe beam is reasonable and the obtained experimental conclusions are applicable to other wavelengths.

By elaborately adjusting the combined concave and convex lenses and the numerical aperture, the probe beam is focused to co-propagate with the filament via a dichroic mirror. The filament diameter is ~100 μm [21], and the diameter of the probe beam is at the same magnitude. An 800-nm filter is placed after the chamber to filter out the high-energy femtosecond laser. The transmissive probe beam is collected by a photodiode (Thorlabs DET10A2, bandwidth 350 MHz) connected with a digital oscilloscope (Tektronix DPO 3034, bandwidth 300 MHz) to record the temporal evolution of the transmitted probe beam, which reflects the formation and relaxation dynamics of channels induced by femtosecond laser filamentation (right inset of Fig. 1). Meanwhile, the modulated spatial profile of the probe beam is also captured by a charge-coupled device (CCD) camera.

Results and Discussion

The filament-induced channel without aerosol inside the cloud chamber is depicted in Fig. 2A. With the presence of the filament, the signals received with and without the probe beam are measured separately. By subtracting the signal without the probe beam, background noise can be removed to obtain the intensity of the probe beam when the filament is present. Then, the filament is turned off and the experiment is repeated to obtain the intensity of the probe beam without the filament. By dividing the probe beam intensity with the filament by that without the filament, the modulation of the probe beam is acquired. The modulation of the probe beam's intensity, which simulates the communication beam in FSOC scenario, describes the transmission efficiency of the filament-induced channel. Figure 2A illustrates the time evolution of probe beam modulation through the filament for varying pulse energies with the repetition rates of 100 Hz. All curves are 10 traces average. The zoomed-in single-pulse dynamics are depicted in Fig. 2B. Clearly, in the absence of aerosols, the influence of the femtosecond laser-induced air channel on the probe beam manifests as an abrupt attenuation and a slow recovery with time. The spatial profiles of the probe beam with and without filaments are also recorded, as shown in the inset of Fig. 2B, which further consolidates the overall attenuating effect of the air channel on the probe laser.

The above attenuation effect can be well attributed to the thermal lensing effect generated by transient laser heating of air during the femtosecond laser filamentation. As the peak power of the pulse exceeds a critical power threshold, the intensity-dependent Kerr optical nonlinearity leads to a positive refractive index increase along the beam axis [36], which acts as a focusing lens that causes the beam to continuously converge. As the pulse self-focuses, its intensity can climb to

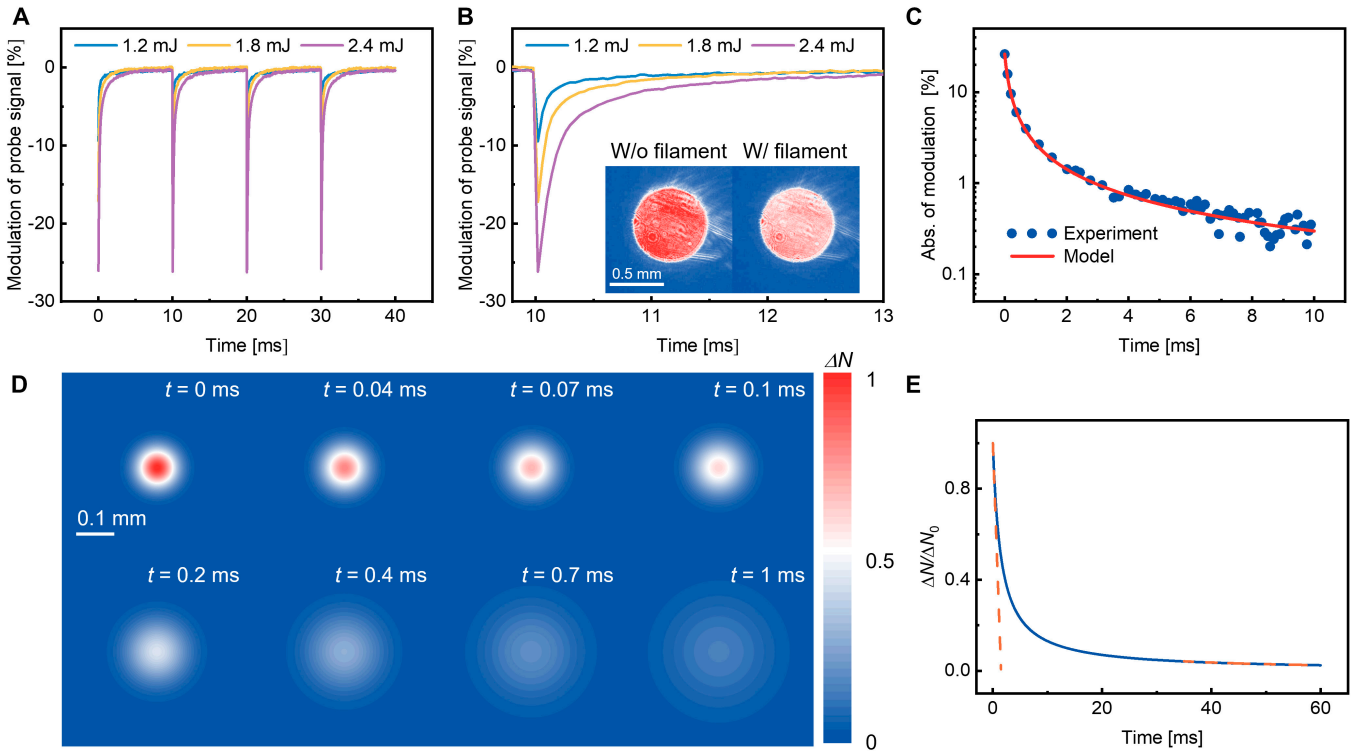

Fig. 2. Dynamics of channel induced by filament without aerosol. (A) Modulation of probe beam as a function of time. (B) Zoomed-in single-pulse dynamics. Inset: Photographs of probe beam light spot without (left) and with (right) filament. (C) Absolute value of modulation for single pulse. Dots and red solid line are experimental and simulation results, respectively. (D) Simulation of number density evolution of air molecules in arbitrary unit at various moments. ΔN represents the normalized air density variation, referenced to the initial central peak density variation at $t = 0$. (E) Simulated relative difference of air molecule number density as a function of time. Dashed lines are the fitting of fast and slow processes.

$\sim 10^{14}$ W/cm^2 and ionization of the medium is triggered [37], depositing free electron plasma, which acts to defocus the beam. Filamentation arises from the resulting dynamic balance between the laser's own self-focusing effect and the defocusing effect generated by the free electron plasma released from ionized molecules [19,20,38]. During filamentation, the ambient gas around the filament is heated and expanded. As the localized temperature sharply rises on axis and subsequently diffuses outward radially, the air molecular density will induce a refractive index change and defocuses the coaxially propagated probe laser, before gradual relaxation restores propagation.

To quantitatively analyze these transient dynamics, we have modeled the filamentation-induced thermal lensing effect based on the heat diffusion equation $\partial T/\partial t = \alpha \nabla^2 T$, where $\alpha = \kappa/c_p$ (κ and c_p are thermal conductivity and specific heat capacity of air, respectively) [39]. According to the second law of thermodynamics, heat will flow from higher temperature bodies to adjacent lower temperature bodies, with the heat transfer rate proportional to the temperature difference and thermal conductivity between the 2 media. It can thus explain conductive thermal effects between air media at different temperatures inside the air channel. After solving for the spatio-temporal evolution of temperature T, the temporal dynamics of air molecule number density can be obtained based on pressure conservation $N(r,t)T(r,t) = N_b T_b$. The finally obtained time-dependent evolution equation for the air molecule number density is:

$$N_{air}(r,t) = N_b T_0 T_b^{-1}\left(R_0^2/\left(R_0^2+4\alpha t\right)\right)\exp\left(-r^2/\left(R_0^2+4\alpha t\right)\right), \quad (1)$$

where α is a constant related to neutral gas thermal conductivity κ and specific heat capacity c_p: $\alpha = \kappa/c_p$. N_b is the ambient air molecule number density, T_0 is the peak temperature increase in the air channel, T_b is the ambient temperature, and R_0 is the initial radius of the air channel, which is assumed to be the same as the radius of the filament $R_0 = 50$ μm. The spatial profiles of gas molecule number density determine the attenuation effect of the probe beam by modulating the refractive index of air.

According to Gladstone–Dale relation [40], the refractive index of air is proportional to air number density $(n-1) \propto N_{air}$, and the proportionality factor is 1.08×10^{-29} m^3 [41]. Since the probe beam is a Gaussian beam, the total beam spread can be expressed as $\theta = 2\lambda/(\pi n \omega_0)$, where λ and ω_0 are the wavelength and waist of the probe beam, respectively. Assuming that the refractive index is uniform and equal to the refractive index at $r = 0$, hence, $N_{air}(t) = N_{air}(0,t) = N_b T_0 T_b^{-1}\left(R_0^2/\left(R_0^2+4\alpha t\right)\right)$, the beam spread difference induced by the refractive index change can be formulated as $\delta\theta = -2\lambda\delta n/(\pi n_0^2 \omega_0)$, where the difference in refractive index is assumed to be small enough to be treated as perturbation. Clearly, the change in air density is proportional to the beam spread of the probe beam, hence proportional to the change in the received signal.

Adopting the relative change in gas molecule number density to represent the induced attenuation effect, the theoretical calculations show good agreement with experimental results, as displayed in Fig. 2C. To effectively demonstrate and emphasize the fitting accuracy across the entire range of modulations, the data are presented in a logarithmic scale; hence, absolute value of modulation in Fig. 2B is employed. To clarify the defocusing effect more intuitively, the spatial distributions of gas density at different moments were calculated and illustrated in Fig. 2D, and the relative difference of air molecule number density was plotted in Fig. 2E. It can be observed that the central gas molecule number density first rapidly diffuses with time, then the diffusion rate notably slows down, revealing that the filament-driven gas diffusion has 2 distinct diffusion velocities with a fast decaying process and a slow decaying process. At the beginning of decaying, $t \approx 0$, air density decays linearly: $\Delta N_{air}(\mathrm{t}) = -4N_b T_0 T_b^{-1}\alpha t / R_0^2$, which is the fast process. At the end of the decaying, R_0^2 is neglectable compared with $4\alpha t$; therefore, $\Delta N_{air}(\mathrm{t}) = N_b T_0 T_b^{-1} R_0^2/(4\alpha t)$. Fitting the fast and slow processes in Fig. 2E enables extracting coefficients required in the thermal diffusion equation. As evident from Fig. 2B, the decay rate of the diffusion process varies with single-pulse energies. This is attributed to the fact that different pulse energies result in varying filament radii, thereby influencing the decay rate.

Subsequently, we perform the similar experiment for the scenario with aerosol inside the cloud chamber imitating fog and clouds in atmosphere. The temporal evolutions of the probe beam transmission through the filament for different pulse energies and the zoomed-in single-pulse dynamics are depicted in Fig. 3A and B, respectively. With the presence of aerosol, the influence of the filament on the probe beam manifests as similar abrupt attenuation at first, but then behaves as an enhancement of the probe beam, and the magnitude of enhancement decreases exponentially over time. The spatial profiles of the probe beam with and without filaments are also depicted in the insets of Fig. 3B, which directly demonstrate the enhancement effect of the femtosecond pulse on the probe beam.

Besides attenuation effect arising from the filament-induced refractive index change, here the enhancement effect stems from the clearing of aerosol droplets by filamentation. The filament creates a shockwave to eject droplets along the filament path and hence improve the transmission of the probe beam. We can use a rate equation to model the dynamics of aerosol droplets [42]:

$$\frac{dN_{drop}(t)}{dt} = \frac{2\left(n_{env} - N_{drop}(t)\right)v_{in}}{\pi R} - \frac{2N_{drop}(t)v_{out}}{R} \quad (2)$$

where n_{env} refers to the aerosol droplet number density in the ambient environment, v_{in} denotes the aerosol injection velocity, v_{out} represents the aerosol diffusion velocity, and R is the radius of the filament. The temporal evolution of the aerosol droplet density described by Eq. 2 contains 2 parts corresponding to aerosol injection and loss. The first injection item stems from diffusion between aerosols inside and outside the air channel, proportional to the aerosol motion velocity, density difference across the channel boundary, and surface area of the filament channel. The second loss item arises from outward diffusion of droplets from the cloud chamber, principally determined by the air channel diameter and diffusion velocity.

This rate equation was numerically solved using the fourth-order Runge–Kutta approach. The simulation result is shown in Fig. 3C. Considering that the attenuation is proportional to the number density change of aerosol, the formula for the modulation of the probe beam by the filament is built as:

$$\frac{I(t)}{I_0} = \frac{1 - A_1 N_1(t)}{1 - A_1}\left(1 - A_2 N_2(t)\right) \quad (3)$$

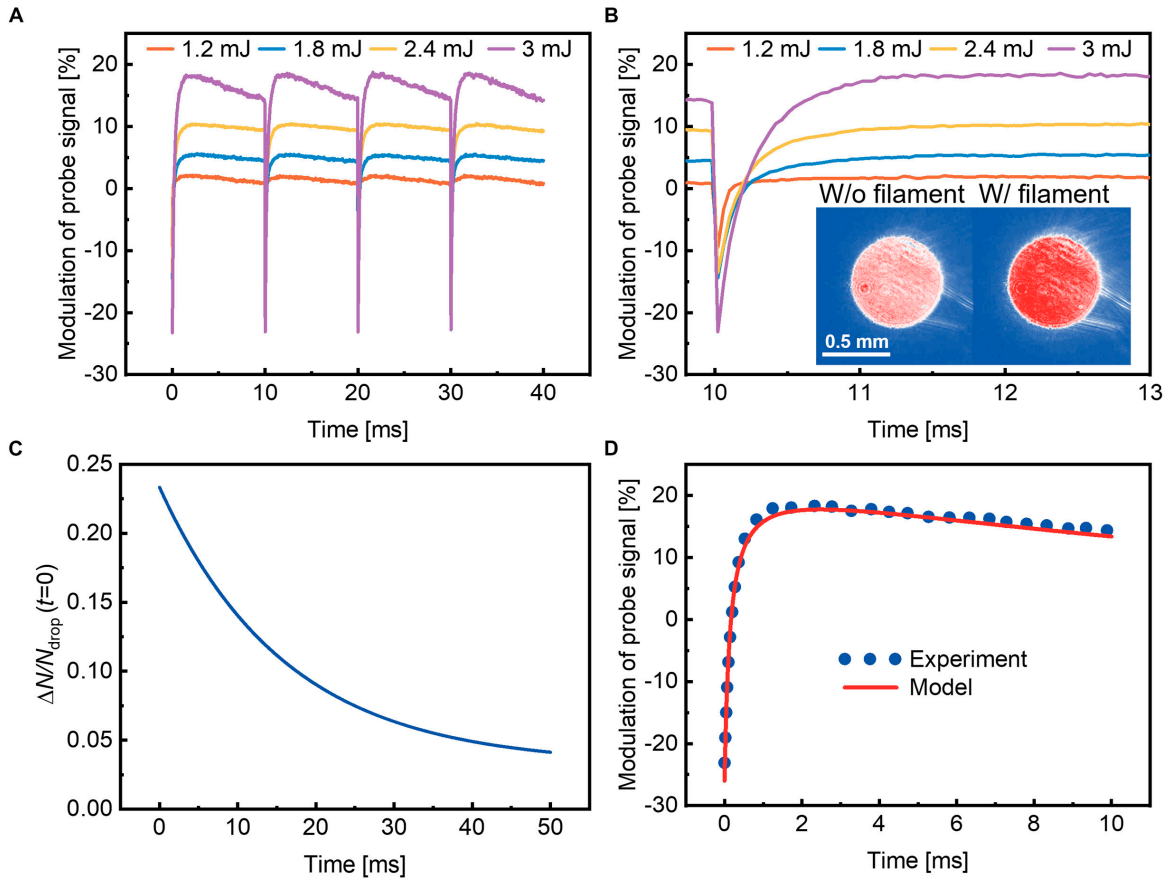

Fig. 3. Dynamics of channel induced by filament with aerosol. (A) Measured modulation of probe beam as a function of time. (B) Zoomed-in single-pulse dynamics. Insets are the photographs of probe beam light spot without filament (left) and with filament (right). (C) Simulation of number density change of aerosol droplets as a function of time. (D) Experimental (dots) and simulation (solid line) results of filament channel dynamics with aerosol.

where $N_1(t) = N_{aero}(t)/N_{aero}(t=0)$ and $N_2(t) = N_{air}(t)/N_{air}(t=0)$ are relative number densities of aerosol and air compared with number densities at initial time $t = 0$. A_1 and A_2 are the extinction coefficients of aerosol and air extracted from the measurement of probe beam absorption with the absence of the filament. Their values are estimated to be 0.3 and 0.4, respectively. When neglecting the existence of aerosol, the first term accounting for aerosol dynamics is effectively negated, and Eq. 3 can be reduced to the case without aerosol. The simulation result of modulation dynamics is shown in Fig. 3D, showing good agreement with experimental results. Note that linear scale is used in Fig. 3D; hence, absolute values are not required as in the case of Fig. 2C.

As observed in Fig. 3B, upon the arrival of the femtosecond laser pulse, the probe beam is diffused with the diffusion decay rate varying for different pulse energies. The trend of the decay rate variation as a function of pulse energies is similar to that in Fig. 2B. This is because, on a very short timescale after the pulse arrival, the power change of the probe beam is dominated by the rapid defocusing effect process. Subsequently, when the rapid defocusing effect ends, the probe beam intensity is governed by the aerosol expulsion effect, manifesting as an enhancement whose amplitude decays exponentially with time. The exponential decay rate slows down with decreasing pulse energy, as lower pulse energies result in an increased initial aerosol concentration, thereby reducing the injection term.

Finally, we explore the effect of repetition rate on the formation and relaxation dynamics of filament channels. As evidenced in Fig. 4, providing the optical power is relatively low, at the same repetition rate of 500 Hz (Fig. 4A) and 900 Hz (Fig. 4B), the attenuation effect arising from defocusing on the probe beam is suppressed and the enhanced transparency due to the droplet expulsion driven by the filament is dominated. As shown in Fig. 4A and B, for the single-pulse energy of 2.5 mJ, only the enhancement of the probe beam (the attenuated thermal defocusing due to the relaxation of the induced negative lens) can be observed. Because the repetition rate is high enough that pulse interval time is smaller than relaxation time of droplets, the attenuation of the probe beam due to the returning of expulsed droplets through diffusion cannot be observed. Moreover, the extracted modulation amplitude exhibits a positive correlation with the single-pulse energy (Fig. 4C), which can be attributed to the fact that higher single-pulse energy leads to higher air temperatures T_0, thereby enhancing the modulation of the refractive index, which in turn amplifies the modulation amplitude. Here, the modulation amplitude represents the span from the minimum to the maximum transmitted intensity of the probe beam, reflecting the transmission of the probe beam influenced by the filament-induced channel. It can be concluded that the pulse energies and repetition frequencies are critical parameters to create a quasi-steady-state channel for communication. Figure 4D and E illustrates the pure gas dynamic without aerosol and the gas and droplet dynamics with aerosol for different

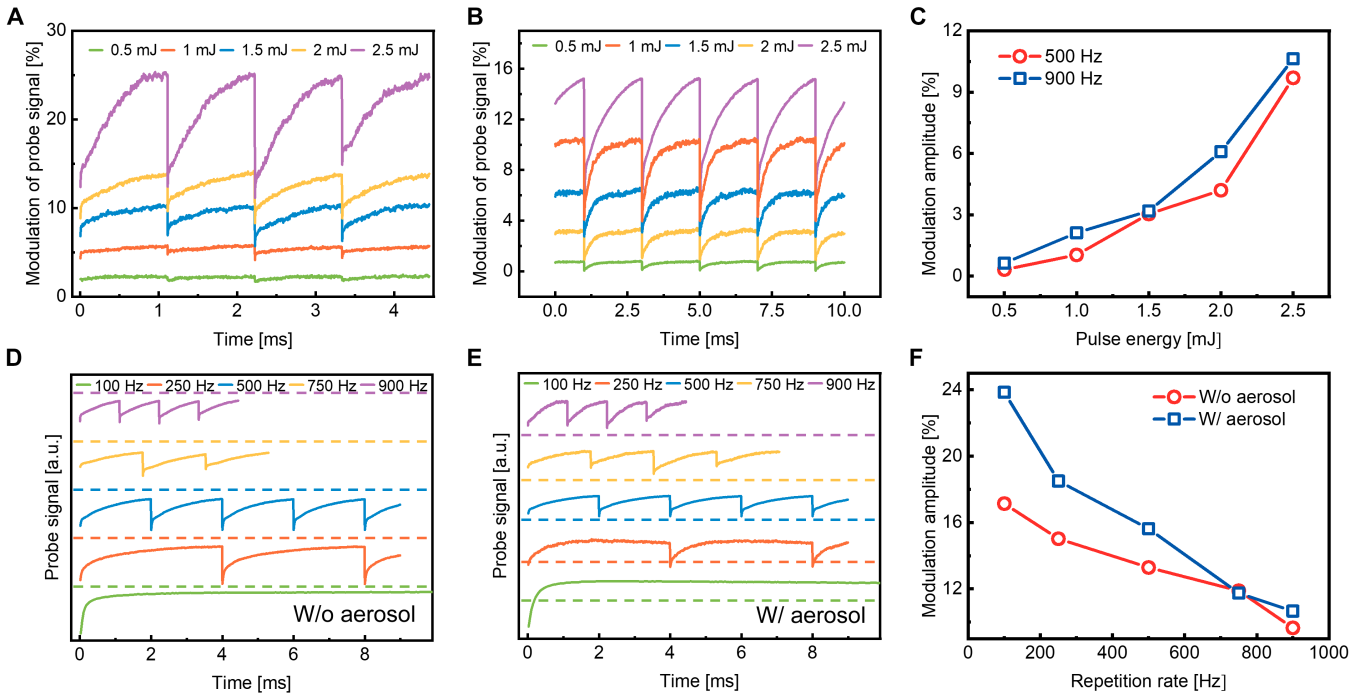

Fig. 4. Dynamics of channel induced by filament for different pulse energies and repetition frequencies. (A and B) Dynamics of filament channel with aerosol at 500 and 900 Hz, respectively. (C) Modulation amplitudes versus pulse energy for repetition rates of 500 Hz (red) and 900 Hz (blue). (D and E) Dynamics of filament channel for various repetition frequencies without (D) and with (E) aerosol at a pulse energy of 2.5 mJ. Dashed line: Zero modulation level. (F) Modulation amplitudes versus repetition rate for filament channel without (red) and with (blue) aerosol.

repetition rates at the fixed pulse energy of 2.5 mJ, respectively. When changing the repetition rate, at high repetition rates, the microsecond-scale thermal defocusing effect dominates, but at lower repetition rates, the influence of the aerosol on the air channel can be discerned. Under fixed pulse energy conditions, higher repetition rates lead to cumulative expulsion effects that tend to overwhelm the contribution of aerosol in evolution of the probe beam signal. Therefore, the relaxed thermal defocusing effect due to the gas diffusion on the microsecond scale determined channel relaxation at high repetition rates, while the influence of the aerosol on the air channel can be discerned at lower repetition rates. The effect of repetition rate on extracted modulation amplitude is also shown in Fig. 4F. Because the attenuation of aerosol contributes an additional component to the modulation amplitude, the modulation amplitude without aerosol is smaller than that with aerosol at different repetition rates. Briefly, the combined effects of gas dynamic-induced thermal defocusing and droplet dynamic-induced scattering attenuation reveal intriguing underlying physics of filament-assisted FSOC through clouds.

Conclusion

In summary, this work has investigated the time evolution of the filament-induced channel in fog under different laser energies and repetition rates and built a combined diffusion model for multiscale and multiphase particles to describe the complex gas and droplet dynamics for filament-assisted FSOC through clouds. Attenuation stemming from heat diffusion was initially observed, followed by enhancement due to shock-wave expulsion of droplets along the filament channel. These results were well explained by simulating the gas density evolution via a heat diffusion model and the aerosol density dynamics through a diffusion equation. Varying optical parameters revealed competitions between thermal and aerosol effects governing channel transmittance. These findings provide insights into the timescales and mechanisms underlying filament-modulated transparency through harsh environments and have directive significance on optimizing filament-assisted FSOC.

Acknowledgments

Funding: This work was supported by the National Natural Science Foundation of China (12074198 and 62105042).
Author contributions: P.Q. and X.L. conceived and supervised the research. H.L. carried out the experiments and simulation. P.Q. and H.L. wrote the manuscript, with feedback from all the authors. J.Z., H.L., J.X., L.L., W.L. and H.J. contributed to the scientific discussions of the results. All authors contributed to the interpretation of the data and the writing of the final manuscript.
Competing interests: The authors declare that they have no competing interests.

Data Availability

Data underlying the results presented in this paper are not publicly available at this time but may be obtained from the authors upon reasonable request.

References

1. Khalighi MA, Uysal M. Survey on free space optical communication: A communication theory perspective. *IEEE Commun Surv Tutor*. 2014;16(4):2231–2258.

2. Cao Z, Zhang X, Osnabrugge G, Li J, Vellekoop IM, Koonen AM. Reconfigurable beam system for non-line-of-sight free-space optical communication. *Light Sci Appl*. 2019;8(1):69.
3. Cheng K, Lu G, Zhu B, Shu L. Polarization changes of partially-coherent Airy-Gaussian beams in a slanted turbulent atmosphere. *Chinese Opt*. 2021;14(2):409–417.
4. Boroson DM, Robinson BS, Murphy DV, Burianek DA, Khatri F, Kovalik JM, Sodnik Z, Cornwell DM. Overview and results of the lunar laser communication demonstration. *Free-Space Laser Commun Atmospheric Propag XXVI*. 2014;8971:213–223.
5. Sodnik Z, Furch B, Lutz H, Free-space laser communication activities in Europe: SILEX and beyond. Paper presented at: LEOS 2006-19th Annual Meeting of the IEEE Lasers and Electro-Optics Society; 2006; Montreal, Quebec, Canada.
6. Samain E, Phung D, Maurice N, Albanesse D, Mariey H, Aimar M, Lagarde G, Vedrenne N, Velluet M, Artaud G. First free space optical communication in Europe between SOTA and MeO optical ground station. Paper presented at: IEEE International Conference on Space Optical Systems and Applications (ICSOS); 2015; New Orleans, LA, USA.
7. Ursin R, Tiefenbacher F, Schmitt-Manderbach T, Weier H, Scheidl T, Lindenthal M, Blauensteiner B, Jennewein T, Perdigues J, Trojek P, et al. Entanglement-based quantum communication over 144 km. *Nat Phys*. 2007;3(7):481–486.
8. Nauerth S, Moll F, Rau M, Fuchs C, Horwath J, Frick S, Weinfurter H. Air-to-ground quantum communication. *Nat Photonics*. 2013;7(5):382–386.
9. Yin J, Cao Y, Li Y, Liao S, Zhang L, Ren J, Cai W, Liu W, Li B, Dai H, et al. Satellite-based entanglement distribution over 1200 kilometers. *Science*. 2017;356(6343):1140–1144.
10. Takenaka H, Carrasco-Casado A, Fujiwara M, Kitamura M, Sasaki M, Toyoshima M. Satellite-to-ground quantum-limited communication using a 50-kg-class microsatellite. *Nat Photonics*. 2017;11(8):502–508.
11. Portnoi M, Haigh PA, Macdonald TJ, Ambroz F, Parkin IP, Darwazeh I, Papakonstantinou I. Bandwidth limits of luminescent solar concentrators as detectors in free-space optical communication systems. *Light Sci Appl*. 2021;10(1):3.
12. Wan Z, Shen Y, Wang Z, Shi Z, Liu Q, Fu X. Divergence-degenerate spatial multiplexing towards future ultrahigh capacity, low error-rate optical communications. *Light Sci Appl*. 2022;11(1):144.
13. Horst Y, Bitachon BI, Kulmer L, Brun J, Blatter T, Conan J-M, Montmerle-Bonnefois A, Montri J, Sorrente B, Lim CB. Tbit/s line-rate satellite feeder links enabled by coherent modulation and full-adaptive optics. *Light Sci Appl*. 2023;12(1):153.
14. Dinu M, Ahrens R, Sochor T, Dailey J, Prego R Jr, Berry M, Crandall L, Kolchmeyer J, Monte A, Engelberth J. Qualification and performance of a high-efficiency laser transmitter for deep-space optical communications. *Free-Space Laser Commun XXXIV*. 2022;11993:129–140.
15. Israel DJ, Edwards BL, Butler RL, Moores JD, Piazzolla S, Du Toit N, Braatz L. Early results from NASA's laser communications relay demonstration (LCRD) experiment program. *Free-Space Laser Commun XXXV*. 2023;12413:10–24.
16. Kwok HS, Rossi T, Lau W, Shaw D. Enhanced transmission in CO2-laser–aerosol interactions. *Opt Lett*. 1988;13(3):192–194.
17. Pustovalov V, Khorunzhii I. Thermal and optical processes in shattering water aerosol droplets by intense optical radiation. *Int J Heat Mass Transf*. 1992;35(2):583–589.
18. Schimmel G, Produit T, Mongin D, Kasparian J, Wolf J-P. Free space laser telecommunication through fog. *Optica*. 2018;5(10):1338–1341.
19. Couairon A, Mysyrowicz A. Femtosecond filamentation in transparent media. *Phys Rep*. 2007;441(2-4):47–189.
20. Bergé L, Skupin S, Nuter R, Kasparian J, Wolf J-P. Ultrashort filaments of light in weakly ionized, optically transparent media. *Rep Prog Phys*. 2007;70(10):1633.
21. Chen Y-H, Varma S, Antonsen T, Milchberg H. Direct measurement of the electron density of extended femtosecond laser pulse-induced filaments. *Phys Rev Lett*. 2010;105(21):Article 215005.
22. Rodriguez M, Bourayou R, Méjean G, Kasparian J, Yu J, Salmon E, Scholz A, Stecklum B, Eislöffel J, Laux U, et al. Kilometer-range nonlinear propagation of femtosecond laser pulses. *Phys Rev E*. 2004;69(3):Article 036607.
23. Kasparian J, Rodríguez M, Méjean G, Yu J, Salmon E, Wille H, Bourayou R, Frey S, André Y-B, Mysyrowicz A. White-light filaments for atmospheric analysis. *Science*. 2003;301(5629):61–64.
24. Mills M, Kolesik M, Christodoulides D. Dressed optical filaments. *Opt Lett*. 2013;38(1):25–27.
25. Kammel R, Ackermann R, Thomas J, Götte J, Skupin S, Tünnermann A, Nolte S. Enhancing precision in fs-laser material processing by simultaneous spatial and temporal focusing. *Light Sci Appl*. 2014;3(5):e169.
26. Zang H, Li H, Zhang W, Fu Y, Chen S, Xu H, Li R. Robust and ultralow-energy-threshold ignition of a lean mixture by an ultrashort-pulsed laser in the filamentation regime. *Light Sci Appl*. 2021;10(1):49.
27. Liu Y, Yin F, Wang T-J, Leng Y, Li R, Xu Z, Chin SL. Stable, intense supercontinuum light generation at 1 kHz by electric field assisted femtosecond laser filamentation in air. *Light Sci Appl*. 2024;13(1):42.
28. Skupin S, Bergé L, Peschel U, Lederer F. Interaction of femtosecond light filaments with obscurants in aerosols. *Phys Rev Lett*. 2004;93(2):Article 023901.
29. Méjean G, Kasparian J, Yu J, Salmon E, Frey S, Wolf J-P, Skupin S, Vinçotte A, Nuter R, Champeaux S. Multifilamentation transmission through fog. *Phys Rev E*. 2005;72(2):Article 026611.
30. Kolesik M, Moloney JV. Self-healing femtosecond light filaments. *Opt Lett*. 2004;29(6):590–592.
31. Courvoisier F, Boutou V, Kasparian J, Salmon E, Méjean G, Yu J, Wolf J-P. Ultraintense light filaments transmitted through clouds. *Appl Phys Lett*. 2003;83(2):213–215.
32. Eisenmann S, Penano J, Sprangle P, Zigler A. Effect of an energy reservoir on the atmospheric propagation of laser-plasma filaments. *Phys Rev Lett*. 2008;100(15):Article 155003.
33. Goffin A, Tartaro A, Milchberg H. Quasi-steady-state air waveguide. *Optica*. 2023;10(4):505–506.
34. Goffin A, Larkin I, Tartaro A, Schweinsberg A, Valenzuela A, Rosenthal E, Milchberg H. Optical guiding in 50-meter-scale air waveguides. *Phys Rev X*. 2023;13(1):Article 011006.
35. Yan B, Liu H, Li C, Jiang X, Li X, Hou J, Zhang H, Lin W, Liu B, Liu J. Laser-filamentation-assisted 1.25 Gb/s video communication under harsh conditions. *Opt Laser Technol*. 2020;131:Article 106391.

36. Polynkin P, Kolesik M. Critical power for self-focusing in the case of ultrashort laser pulses. *Phys Rev A*. 2013;87(5):Article 053829.
37. Xu S, Bernhardt J, Sharifi M, Liu W, Chin S. Intensity clamping during laser filamentation by TW level femtosecond laser in air and argon. *Laser Phys*. 2012;22:195–202.
38. Braun A, Korn G, Liu X, Du D, Squier J, Mourou G. Self-channeling of high-peak-power femtosecond laser pulses in air. *Opt Lett*. 1995;20(1):73–75.
39. Cheng Y-H, Wahlstrand J, Jhajj N, Milchberg H. The effect of long timescale gas dynamics on femtosecond filamentation. *Opt Express*. 2013;21(4):4740–4751.
40. Gladstone JH, Dale TP, XIV. Researches on the refraction, dispersion, and sensitiveness of liquids. *Philos Trans R Soc Lond*. 1863;153:317–343.
41. Qin X, Xiao X, Puri IK, Aggarwal SK. Effect of varying composition on temperature reconstructions obtained from refractive index measurements in flames. *Combust Flame*. 2002;128(1-2):121–132.
42. de la Cruz L, Schubert E, Mongin D, Klingebiel S, Schultze M, Metzger T, Michel K, Kasparian J, Wolf J.-P, High repetition rate ultrashort laser cuts a path through fog. *Appl Phys Lett* 2016;109(25):251105.